

Unsteady Aerodynamic effects in small-amplitude pitch oscillations of an airfoil

P. S. Negi, R. Vinuesa, A. Hanifi, P. Schlatter and D. S. Henningson

Linné FLOW Centre, KTH Mechanics, S-100 44 Stockholm, Sweden
Swedish e-Science Research Centre (SeRC), SE-100 44, Stockholm, Sweden

Submitted to International Journal of Heat and Fluid Flow

Wall-resolved large-eddy simulations (LES) are utilized to investigate the flow-physics of small-amplitude pitch oscillations of an airfoil at $Re_c = 100,000$, and with a reduced frequency $k = 0.5$. The investigation of the unsteady phenomenon is done in the context of a natural laminar flow airfoils, which can display sensitive dependence of the aerodynamic forces on the angle of attack in certain “off-design” conditions. The dynamic range of the pitch oscillations is chosen to be in this sensitive region, which sees the destabilization and disappearance of a laminar separation bubble at the leading edge. The transition point on the suction-side is seen to constantly change during the pitch cycle, resulting in a dynamically rich flow response, as well as large asymmetry of boundary over airfoil between the pitch-up and pitch-down motions. A relaxation-term (RT) based LES procedure is employed which adds small amount of dissipation in the smallest resolved scales to account for the dissipation from the unresolved small scales. Validation of the procedure is presented for turbulent channel flows and for flow around a wing section.

Key words: aerodynamics, dynamic-response, transition

1. Introduction

A large focus of the studies unsteady wings tends towards large pitch amplitudes and stall dynamics such as the early works of McCroskey (1981); McCroskey *et al.* (1982); McCroskey (1973); McCroskey *et al.* (1976); Carr *et al.* (1977) etc. More recent works by Dunne & McKeon (2015), Rival & Tropea (2010), Choudhry *et al.* (2014) etc. continue the investigation of the process which appears far from complete. The review by McCroskey (1982) and a more recent one by Coorke & Thomas (2015) provide an overview of the development of unsteady airfoil behavior related to dynamic stall. Much lesser attention has gone towards studying unsteady aerodynamic behavior in the cases of small pitch amplitudes. Some works dealing with small pitch amplitudes include the work done by Pascazio *et al.* (1996) which shows a time delay in laminar-turbulent transition

during pitching. Nati *et al.* (2015) study the effect of small amplitude pitching on a laminar separation bubble at low Reynolds numbers. Such cases qualitatively

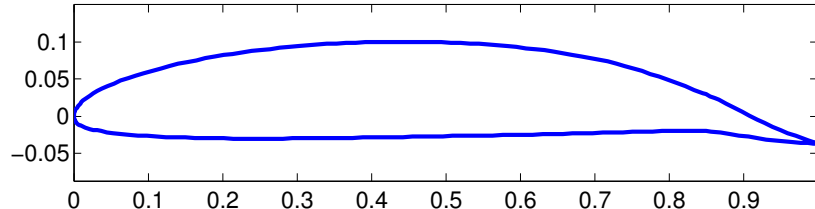


Figure 1: Natural Laminar Flow (NLF) airfoil extensively tested at the Aeronautical and Vehicle engineering department of KTH (Lokatt & Eller 2017; Lokatt 2017)

represent small changes in operating conditions, such as structural deformations or small trailing edge flap deflections. The understanding of flow response to such changes can be crucial in cases where small perturbations induce large changes in aerodynamic forces. Natural laminar flow (NLF) airfoils may display such sensitive dependence of aerodynamic characteristics for a certain range of angle of attack *viz.* the operating conditions. Their performance critically depends on maintaining laminar flow over the suction side of the airfoil and a loss of laminar flow over the airfoil causes large variations of the aerodynamic forces. Recently Mai & Hebler (2011), and Hebler *et al.* (2013) have performed unsteady experiments on natural laminar flows in the transonic range and have found non-linearities in the dynamic response of the normal force coefficients. Lokatt (2017) have performed similar experiments within the subsonic range and found strongly non-linear behavior of the normal force coefficient. The non-linearities have been strongly linked to the free movement of transition over the suction side of the airfoil and they appear to be nearly absent when suction side transition is fixed at the leading-edge (Mai & Hebler 2011; Lokatt 2017).

The current work investigates the effect of small-amplitude pitch oscillations on one such laminar airfoil (figure 1). The airfoil was designed at the Aeronautical and Vehicle Engineering department of KTH where it has been used in some experimental and numerical works (Lokatt & Eller 2017) and is the same airfoil used in the unsteady experiments of Lokatt (2017). The simulations were performed at a chord-based Reynolds number of $Re_c = 100,000$ within the α range where the above mentioned sensitivity of aerodynamic characteristics to small changes in angle of attack is observed. The sensitive α range for this Reynolds number was determined with calculations using an integral boundary layer code, Xfoil, Drela (1989), which predicted sharp changes in the coefficient of moment (C_m) and suction side transition location (figure 2) above an angle of attack $\alpha > 6^\circ$.

In recent works, wall-resolved large-eddy simulations have proven to be an effective tool for studying flow physics at high Reynolds numbers but with a computational cost which is much lower than that of direct numerical simulations



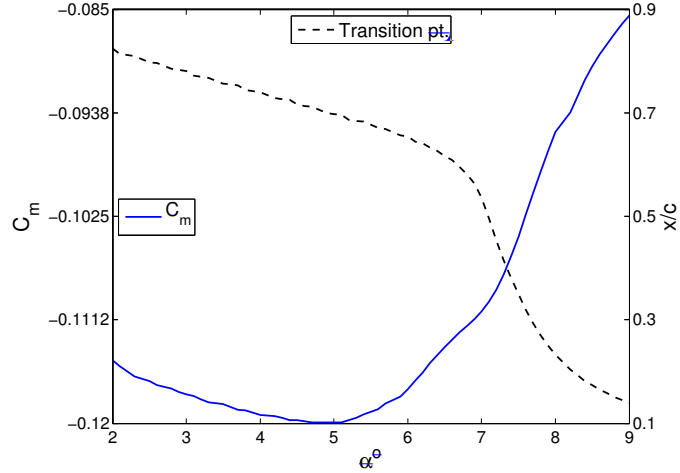


Figure 2: Coefficient of moment (C_m), displayed on the left axis, and suction side transition location, shown on the right axis. Values obtained using Xfoil.

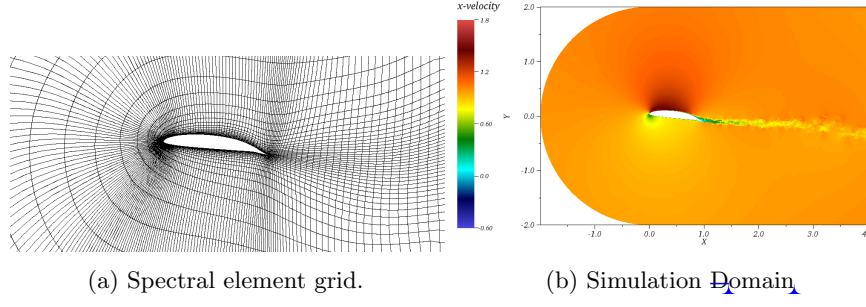


Figure 3: (a) A close-up of the spectral element grid near the airfoil surface. (b) 2D section of the simulation domain: Outflow boundary is 4 chords downstream of the airfoil leading edge while the inflow boundary is 2 chords away. Colored region represents the instantaneous streamwise velocity.

(DNS). Some of the works to utilize this method include spatially evolving boundary layers (Etel-Amor *et al.* 2014), pipe flows (Chin *et al.* 2015) and flow over wings (Uzun & Hussaini 2010; Lombard *et al.* 2016). Successful application of the approach has motivated its use in the present work which aims to gain insight into the flow-physics of unsteady airfoils undergoing small amplitude pitch oscillations.

2. Numerical Method

The computational code used for the simulations is Nek5000, which is an open source research code developed by Fischer *et al.* (2008) at Argonne National Laboratory. It is based on a spectral-element method which allows the mapping

of elements to complex geometries along with a high order spatial discretization within the elements. The method uses Lagrange interpolants of orthogonal Legendre polynomials as basis functions and utilizes Gauss–Lobatto–Legendre (GLL) quadrature for the distribution of points within the elements. The spatial discretization is done by means of the Galerkin approximation, following the $P_N - P_{N-2}$ formulation. An 11th order polynomial approximation is used for the velocity with a 9th order approximation for pressure. The nonlinear terms are treated explicitly by third-order extrapolation (EXT3), whereas the viscous terms are treated implicitly by a third-order backward differentiation scheme (BDF3). Aliasing errors are removed with the use of over-integration. All equations are solved in non-dimensional units with the velocities normalized by the reference free-stream velocity U_0 and the length scales in all directions are normalized by the chord length c . The resultant non-dimensional time unit is given by c/U_0 .

2.1. Relaxation-term large-eddy simulation (RT-LES)

The LES method is based on the RT3D variant of the ADM-RT approach first used by Schlatter *et al.* (2004). The method supplements the governing equations with a dissipative term $(\chi \mathcal{H}(u))$. The equations of motion for the resolved velocity and pressure thus read:

$$\frac{\partial u}{\partial t} + u \cdot \nabla u = -\frac{1}{\rho} \nabla p + \frac{1}{Re} \nabla^2 u - \chi \mathcal{H}(u) \quad (1)$$

$$\nabla \cdot u = 0 \quad (2)$$

where \mathcal{H} is a defined high-pass spectral filter and χ is a model parameter which together with \mathcal{H} determines the strength of the dissipative term. The method has been used in earlier studies of boundary layer simulations in Eitel-Amor *et al.* (2014) and channel flows in Schlatter *et al.* (2006), and has been shown to be reliable in predicting transition location and also preserving the characteristic structures which are seen in the DNS of transitional flows by Schlatter *et al.* (2006).

2.2. Computational Setup

A number of tests were carried out in a channel flow at a friction Reynolds number of $Re_\tau = 395$, and the results are compared with the DNS data of Moser *et al.* (1999). Finally the chosen resolution was set to $\Delta x^+ = 18$, $\Delta z^+ = 9$, with the first point in the wall-normal direction set at $\Delta y_w^+ = 0.64$ and the wall-normal resolution near the boundary layer edge is set to $y_{max}^+ = 11$. The superscript $+$ indicates normalization in inner units. The resolution is very similar to the one used in Eitel-Amor *et al.* (2014) where the ADM-RT model is also used to simulate a spatially evolving boundary layer. A comparison of the results for the turbulent channel flow is shown for the mean velocity in figure 4a, and for the turbulent kinetic energy budget (TKE) in figure 4b. The dissipation profile shown in the figure is the sum of resolved dissipation and the added dissipation by the relaxation term. A very good agreement with the

DNS is found for the mean velocity and all the kinetic energy budget terms (including the total dissipation).

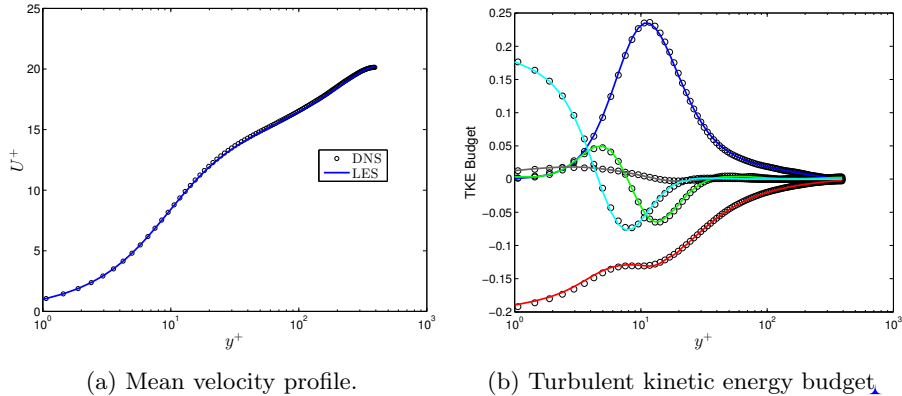


Figure 4: Comparison of mean velocity profile and turbulent kinetic energy budget. Circles represent the DNS data from Moser *et al.* (1999) while the lines represent the values from the LES. All values are normalized with inner units. The individual terms for the turbulent kinetic energy budget in (b) are color coded as: Production, Dissipation, Viscous diffusion, Turbulent diffusion, Velocity-Pressure correlation.

The same resolution (in inner units) is then used to design the mesh around the airfoil, with additional care taken for special regions like the leading and trailing edge. Wall-shear stress data is obtained using Xfoil to estimate the grid spacing on the airfoil. A trip is introduced in Xfoil at $x/c \approx 0.1$ to obtain turbulent wall-shear values on both the suction and pressure sides of the airfoil. Here c denotes the chord length. Finally, the grid design uses the following criteria:

- For $0.1 < x/c < 0.6$, $\Delta x^+ = 18$, $\Delta y_{wall}^+ = 0.64$ and $\Delta y_{max}^+ = 11$, using the local wall-shear (τ_w) values on the airfoil. Since the flow is expected to be laminar on the pressure side, the stream-wise resolution is slightly relaxed to $\Delta x^+ = 25$ while keeping the same wall-normal resolution.
- For $x/c < 0.1$, the peak τ_w value over the suction side of the airfoil is used to estimate the grid spacing.
- For $x/c > 0.6$, the suction side experiences a large adverse pressure gradient which significantly reduces τ_w values. Therefore, the τ_w values from the pressure side are used for both the suction and pressure sides.
- A structured mesh is used, which is extruded in the span-wise direction. Hence the spanwise resolution is constant throughout the domain. The resolution is set to $\Delta z^+ = 9$, where the peak τ_w value from the suction side is used.

A different criterion is needed for defining the resolution in the wake where the wall-based criteria are not valid. Accordingly, RANS simulations were

performed using *ANSYS[®] FLUENT*, Academic Research, Release 16.1, to estimate the Kolmogorov length scale (η) in the wake region. The grid in the wake region is designed such that the average grid spacing between the GLL points follows the criteria: $\Delta x/\eta < 9$. The far field boundaries are 2 chords away from the airfoil leading edge in either direction and the outflow boundary is 4 chords downstream from the airfoil leading edge. The inlet is designed as a curved inflow boundary with a constant radial distance of 2 chords from the leading edge of the airfoil. The computational domain is 0.25 chords wide in the spanwise direction. The domain can be visualized in figure 3b. The spectral-elements can be visualized in the close-up view (figure 3a). Each of the spectral-elements are further discretized by $12 \times 12 \times 12$ grid points in 3D, corresponding to an 11th order spectral discretization. Periodic boundary conditions are imposed on the spanwise boundaries, while the energy-stabilized outflow condition suggested by Dong *et al.* (2014) is imposed on the outflow boundary. This outflow condition was shown to be accurate and stable in flows with strong back-flow velocities at the outflow boundary by Dong *et al.* (2014). Velocity field data is extracted from an unsteady RANS simulation and the time-averaged value is interpolated onto the domain inlet and far-field boundaries. The interpolated data is then imposed as a Dirichlet boundary condition on these boundaries. The method is very similar to the one used by Hosseini *et al.* (2016) in their DNS of flow around a wing section. In order to simulate low turbulence flight conditions, free-stream turbulence of intensity $Ti = 0.1\%$ is superimposed on the Dirichlet boundary conditions. The free-stream turbulence is generated using Fourier modes with a von Kármán spectrum. The procedure is similar to the one described in Brandt *et al.* (2004) and has been used for the study of transition in flat plate boundary layers under the influence of free-stream turbulence.

A validation of the above criterion for complex geometries such as a wing section was performed at a chord based Reynolds number of $Re_c = 400,000$ for NACA4412 airfoil. The LES grid resolution was setup with the same grid criteria as described above. The domain boundaries and boundary conditions are identical to the setup in Hosseini *et al.* (2016). The results are validated using the DNS data from Hosseini *et al.* (2016). Wall-normal profiles of the normalized kinetic energy budget is shown in figure 5. The profiles are extracted a streamwise location of $x/c = 0.7$ on the suction side of the airfoil. The LES profiles (lines) match very well with the DNS data (circles), signifying the high accuracy of the LES with the current resolution.

3. Results and discussion

3.1. Steady results

Simulations with a stationary airfoil were performed to investigate the location of transition without pitching motion. The simulations were performed for $Re_c = 100,000$ at two different angles of attack ($\alpha = 6.7^\circ$ and $\alpha = 8.0^\circ$). As observed in figure 6, the iso-contours of coherent structures, identified by

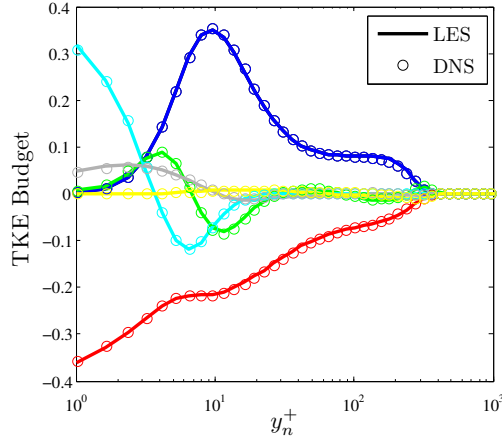


Figure 5: Comparison of turbulent kinetic energy budget for a NACA4412 wing section at the suction side location of $x/c = 0.7$. The circles represent DNS data from Hosseini *et al.* (2016) while the lines are data from the LES. The individual terms are color coded as: Production, Dissipation, Viscous diffusion, Turbulent diffusion, Velocity-Pressure correlation,

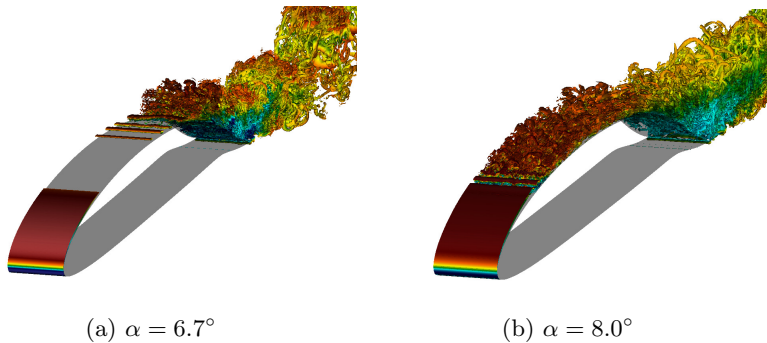


Figure 6: Isocontours of instantaneous λ_2 structures observed for two different (steady) angles of attack.

negative λ_2 (Jeong & Hussain 1995), show a substantial change in transition location for a small $\Delta\alpha = 1.3^\circ$. For $\alpha = 6.7^\circ$ the transition is close to the trailing edge at $x/c \approx 0.7$, where due to the effects of strong pressure gradient a small laminar separation bubble develops near $x/c \approx 0.6$ and the flow transition occurs at $x/c \approx 0.7$. While for $\alpha = 8.0^\circ$, a leading-edge laminar separation bubble forms, causing flow transition much closer to the leading edge at $x/c \approx 0.2$. Such a leading-edge laminar separation bubble is not observed for the $\alpha = 6.7^\circ$ case. The results are consistent with the trends obtained from Xfoil calculations,

showing a large variation in the transition point within a small α change (figure 2).

3.2. Pitching results

Once the transition change is established in the steady simulations, the airfoil is then pitched about a mean $\alpha_0 = 6.7^\circ$ with a pitching amplitude of $\Delta\alpha = 1.3^\circ$ and a reduced frequency of $k = 0.5$ about a pitch axis of $(x_0, y_0) = (0.35, 0.034)$. Where, $k = \frac{\omega c}{2U_0}$ with ω being the angular frequency of oscillation. The motion of the airfoil is prescribed by equation 3. The pitching motion corresponds to an oscillation time period of $T_{osc} = 2\pi$.

$$\alpha = \alpha_0 + \Delta\alpha \sin(\omega t) \quad (3)$$

The time variation of the coefficient of lift (C_L) is shown in figure 7 where the blue line shows the C_L values and the dashed black line shows the variation of α with time. The initial phase of pitching motion is carried out using a lower resolution (polynomial order $N = 5$) to simulate the initial transient period of the flow at a lower computational cost. The polynomial order is then smoothly raised to $N = 11$ before the fourth pitch cycle. Due to the fairly large separation at the trailing edge, effects of transition movement and turbulence, successive pitch cycles are not expected to have identical behavior, however some of qualitatively repeating trends can be observed. The behavior of the lift coefficient shows a chaotic but qualitatively repeating pattern where the lift coefficient shows a fairly smooth increase during the pitch-up motion, with strong secondary effects occurring near the maximum of the pitch cycles. Similarly in the pitch-down phase the lift decreases smoothly with secondary effects again becoming important at the minima of the pitch-cycle.

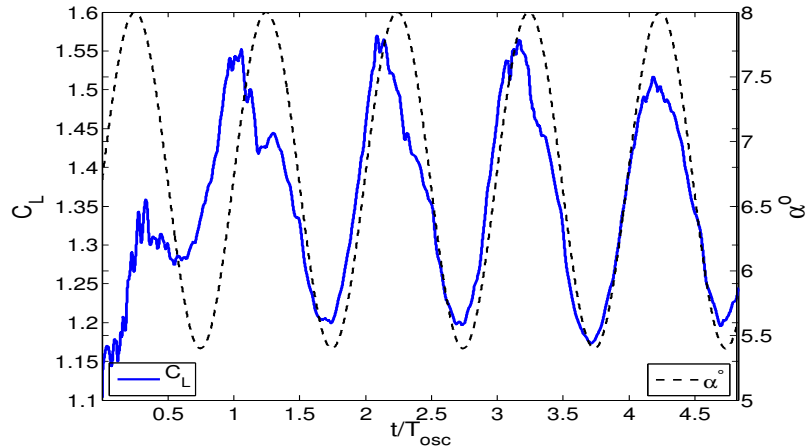


Figure 7: Coefficient of Lift (C_L) and angle of attack (α) variation with time. C_L is on the left axes while α is on the right axes.

In order to understand the time variation of the spatially developing boundary layer on the airfoil, we look at the space-time evolution of the instantaneous spanwise averaged wall-shear stress. The space-time surface plot is shown in figure 8a, which spans the fourth and fifth pitch cycles. The x -axis indicates the chord-wise location on the suction side of the airfoil while the y -axis indicates the simulation time normalized with the time period of oscillation (T_{osc}). The color specifies the value of wall-shear stress on the suction side of the airfoil. Regions with color intensity strongly towards red are indicative of high shear and thus turbulent flow. The exception to the rule being the region close to the leading edge where the flow is laminar but a high shear region exists due to the extremely thin boundary layer close to the stagnation point. The same space-time surface is plotted again as a binary colored surface plot in figure 8b, where black colored regions indicate negative wall-shear stress and hence separated flow, while the white region corresponds to locations with attached flow ($\tau_w > 0$). Horizontal dashed lines mark specific phases of the pitch cycle. Red dashed line indicates mean instantaneous angle of attack, while blue dashed lines indicate the extreme positions of the instantaneous angle of attack.

It is obvious from the two plots in figure 8, that the developing boundary layer on the airfoil exhibits a dynamically rich response to small-amplitude pitch oscillations, with different key boundary layer characteristics controlling the dynamics of the flow in different phases of the pitch cycle. We briefly identify some of the key boundary layer characteristics to paint an over-all picture of the dynamics. A persistent trailing edge separation can be identified in figure 8b beyond $x/c > 0.8$. The trailing-edge separation is does not exhibit reverse flow 100% of the time, as can be seen from the white patches dispersed between largely black colored regions. An isolated separated region (distinct from the trailing edge separation) is seen at $x/c \approx 0.6$ at times $t/T_{osc} \approx 3$ and $t/T_{osc} \approx 4$. This is identified as a trailing-edge LSB. This LSB is short lived in time, existing for slightly less than a quarter of the pitch-cycle. A large separated region near the leading edge is a leading-edge LSB, similar to the one seen in the steady case at $\alpha = 8.0^\circ$. The separation bubble persists much longer in time, spanning nearly half a pitch cycle. Thus the flow dynamics may broadly be described as an oscillation between states corresponding to the leading edge and trailing edge laminar separation bubbles. Evident from figure 8a is that the transition point changes substantially throughout the pitch cycle. Interestingly, the flow over the airfoil is substantially different between the pitch-up and the pitch-down phases for the same angle of attack. For example, when the instantaneous angle of attack is at phase $\phi = 0$ ($t/T_{osc} = 3, 4$), which represents mean angle of attack but in the pitch-up phase, the flow over the airfoil is mostly laminar up till $x/c \approx 0.7$. On the other hand, for a phase of $\phi = \pi$ ($t/T_{osc} = 3.5, 4.5$), representing the airfoil at the mean angle of attack but in the pitch-down phase, the flow is almost entirely turbulent with the start of the turbulent region approximately at $x/c \approx 0.25$.

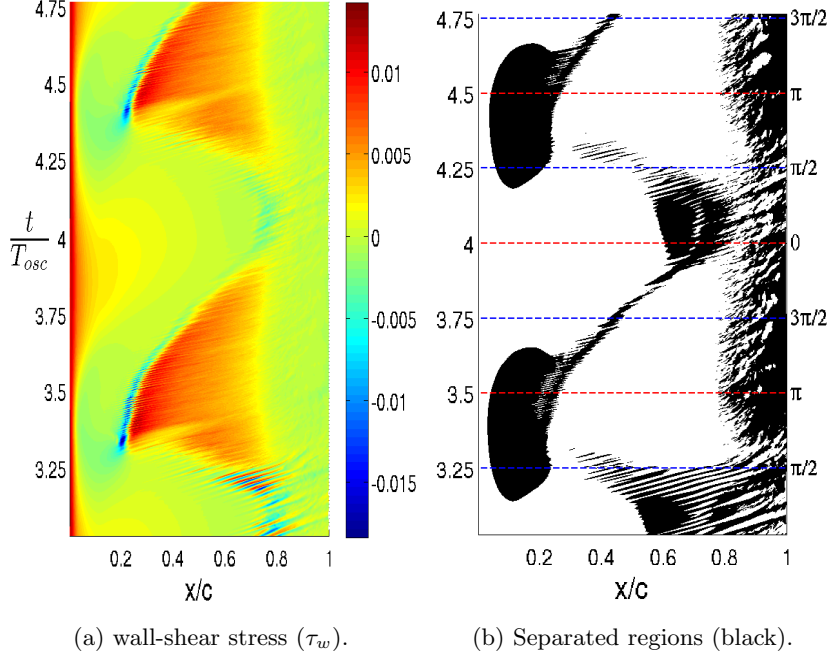


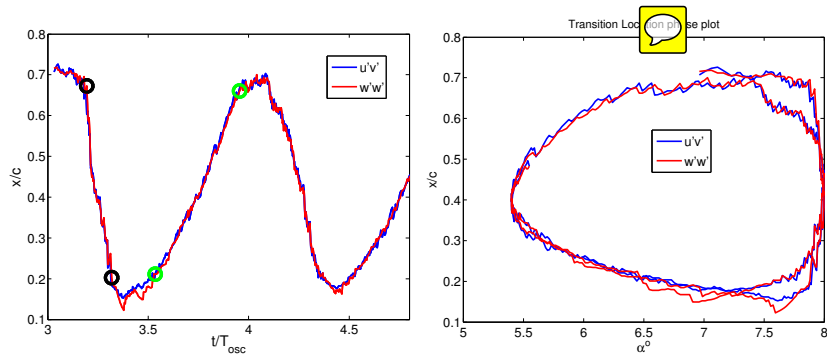
Figure 8: Space-time plot for the wall-shear values (τ_w) and separated flow regions. The values are obtained from the instantaneous flow averaged over the spanwise direction. Horizontal blue dashed lines in 8b represent the ~~extremum~~ positions of angle of attack, while the red dashed lines represent phases corresponding to mean angle of attack.

In the ~~current~~ work we focus on the variation of transition location throughout the pitch cycles. Since the flow case is unsteady, and the transition location does not remain fixed, the standard procedure of specifying transition location using flow intermittency is no longer feasible and a different ~~criteria~~ is needed to determine the instantaneous transition location. In order to determine ~~transition~~, we calculated flow statistics which are averaged in the homogeneous spanwise direction, and also averaged for a short duration (Δt) in time. Thus the instantaneous value of any statistical quantity " $\bar{q}(x, y, t)$ " can be evaluated as in equation 4:

$$\bar{q}(x, y, t) = \left(\frac{1}{z_{max} - z_{min}} \right) \left(\frac{1}{\Delta t} \right) \int_{t'=t}^{t'=t+\Delta t} \int_{z=z_{min}}^{z=z_{max}} q(x, y, z, t') dz dt' \quad (4)$$

In order for such a quantity to be representative of the instantaneous state of the flow, the time duration of the averaging must be small. For the current case we use $\Delta t = 4 \times 10^{-3}$, which amounts to 0.06% of the oscillation time period during which the flow can be assumed to remain in the same state. Using this procedure we evaluate the fluctuating Reynolds stress, $\overline{u'v'}(x, y, t)$, in order

to determine the instantaneous transition location. Within the boundary layer region ~~above~~ the suction-side, the location where the absolute value of ~~the~~ quantity first becomes larger than a certain threshold, that point is denoted as the ~~transition~~ point. In order to prescribe a suitable threshold, the maximum value of $|u'v'(x, y, t)|$ across the entire boundary layer is evaluated ~~for all times~~. This maximum value does not ~~have~~ very large variations ~~staying~~ within the same order of magnitude for all times with its mean value being $\overline{|u'v'|}_{max} = 0.05$. The threshold for determining transition is set to 5% of this value. The transition point is thus the first point where $|u'v'(x, y, t)| > 0.0025$. Since we use an ad-hoc ~~criteria~~ for transition location, this is cross-checked by evaluating the variance of the spanwise velocity fluctuations $\overline{w'w'}(x, y, t)$, and following an identical procedure as described above. In this case the transition ~~criteria~~ is prescribed as $|\overline{w'w'}(x, y, t)| > 0.005$ since the peak spanwise fluctuation intensities are found to be higher than the peak Reynolds stress $|\overline{u'v'}|$. Physically, growing spanwise velocity fluctuations indicate the onset of three-dimensionality in the boundary layer, ~~which are~~ associated with secondary instabilities. While the ~~thresholds specified~~ may be considered ad-hoc, the qualitative picture of transition movement is not very sensitive to small changes in the threshold. Reducing the thresholds by a factor of 2 still produces the same qualitative trends (not shown). Figure 10 shows the calculated transition locations overlayed on the wall-shear stress and separation space-time plots. The calculated transition locations are consistent with the picture of wall-shear stress with transition marginally preceding regions of turbulent flow. Moreover, the time variation of transition point determined by two different physical quantities agree very well with each other. Thus we consider the ~~quantities as a good representation~~ of changing flow characteristics.



(a) Transition variation with time. (b) Transition location phase portrait.

Figure 9: Time variation (a) and phase portrait with α (b) of transition location evaluated using the criteria for $|u'v'|$ and $|w'w'|$. The circles ~~mark~~ the points used to approximate the upstream (black circles) and downstream (green circles) velocities of the transition point.

The overlay plots in figure 10 clearly indicate that the two LSBs play a **dominating** role in the flow dynamics and that transition location is governed by the characteristics of these LSBs. Figure 11 shows the instantaneous iso-contours of the λ_2 structures at four different times during the pitch-up cycle when the transition is moving upstream. The top figure shows the flow state near the mean angle of attack ($t/T_{osc} = 3.09$) during the pitch-up phase. The flow is mostly laminar across the wing with no structures **seen** prior to flow transition. The high adverse pressure gradient near the trailing edge causes the laminar flow to easily separate, forming a laminar separation bubble and flow transitions over this separated shear layer. The next figure from the top is at the time instant $t/T_{osc} = 3.2$ and the leading edge LSB has formed which excites spatially growing waves as seen by the quasi two-dimensional vortical structures captured by the λ_2 **criteria**. As the LSB grows in size, the spatially growing waves undergo stronger amplification and transition downstream of the leading-edge LSB (third figure from top at $t/T_{osc} = 3.3$). The flow downstream of the point of transition is now turbulent and thus does not separate from the surface. The LSB near the trailing edge therefore ceases to exist. Finally, the leading-edge LSB **grows** large enough that flow transitions within this separated shear layer (bottom figure at $t/T_{osc} = 3.47$). The growth of the leading-edge LSB can be quantified in terms of the maximum reverse flow observed within recirculation region. Figure 12 shows the absolute value of the maximum reverse flow within the circulation region normalized by the free-stream velocity at the boundary layer edge. Alam & Sandham (2000) with their local stability analysis of a two-parameter family of reverse flow profiles indicated that reverse flow intensities above 15% may cause the flow to be locally absolutely unstable. With a similar analysis on a three parameter family of profiles Hammond & Redekopp (1998) obtained onset of absolute instabilities at 20% reverse flow velocities. The authors also performed global stability analysis on a synthetically **created** boundary layer with a symmetric separation bubble (Hammond & Redekopp 1998) and found the flow to be globally unstable for 30% reverse flow velocities. In the current flow case reverse flow intensities of up to 40% can be observed shortly before transition occurs within the separated shear layer of the leading edge LSB. This is much higher than the onset of absolute instability reported in the earlier studies and while we do not perform a formal stability analysis in the current study, it is reasonable to assume the leading-edge LSB becomes globally unstable, and causes transition at the separated shear layer.

During the pitch down phase of the oscillation cycle, the leading-edge LSB shrinks in size and eventually ceases to be globally unstable. The transition point then starts moving downstream from the leading-edge LSB and the flow over the airfoil begins a slow re-laminarization process. There is a marked asymmetry between the upstream and downstream movement of the transition point. An approximate velocity for both the upstream and downstream motion of the transition point is calculated across the points marked by circles in figure 9a which correspond to transition movement with near constant velocity. The velocity of upstream transition movement is calculated across the black

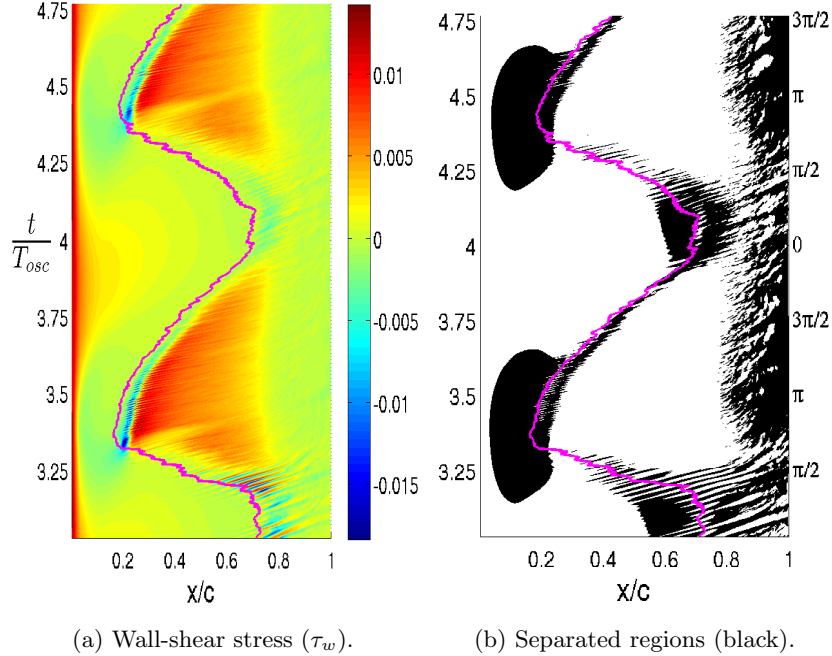


Figure 10: Transition locations indicated by the magenta line overlaid on the space-time plots of wall-shear stress and separation.

circles and is equal to $V_u^{tr} = -0.60$, while the velocity of the downstream motion of transition is calculated across the green circles and is equal to $V_d^{tr} = 0.17$. Thus the upstream spread of turbulent regions is much faster than the re-laminarization. At the moment it is unclear what causes the asymmetry between the upstream and downstream movement of transition, or if symmetric movement can even be expected. The cause of this asymmetry will be the focus of future work.

4. Conclusion

A relaxation-term filtering procedure is used for wall-resolved LES of flow over a pitching airfoil. The procedure supplements the Navier–Stokes equations with a relaxation term which adds dissipation in the smallest resolved scales of the flow. Validation of the LES procedure is done in a channel flow at $Re_\tau = 395$ and for a wing section at $Re_c = 400,000$ and the results show a very good agreement with available DNS data sets.

Flow over an airfoil is simulated using the LES procedure at a chord-based Reynolds number of $Re_c = 100,000$ within an angle of attack range where the aerodynamic forces on the airfoil exhibit sensitive dependence on the angle of attack. This sensitive dependence is captured in the steady simulations at

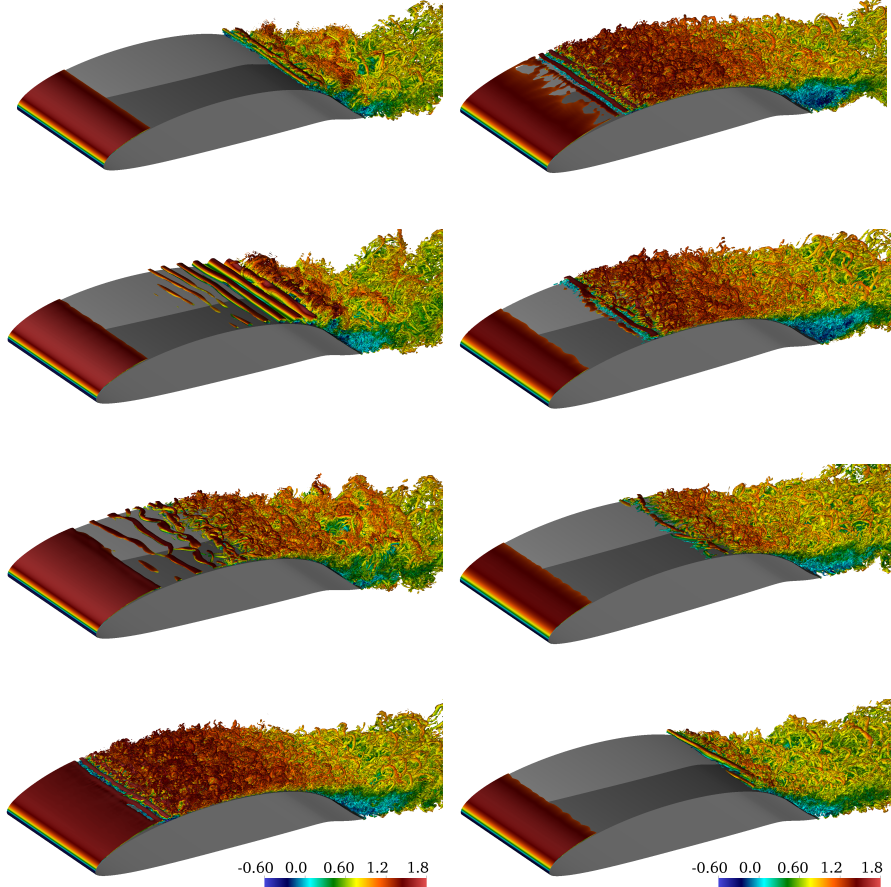


Figure 11: Visualization of instantaneous λ_2 structure during different phases of the pitch cycle. The figures on the left are during the phase of the pitch cycle when the transition is moving upstream. From top to bottom the time-stamps of the instantaneous snapshots correspond to a normalized flow time of $t/T_{osc} = 3.09, 3.2, 3.3, 3.47$. On the right the instantaneous snapshot correspond to the re-laminarization phase as transition moves downstream. The time-stamps from top to bottom on the right correspond to $t/T_{osc} = 3.55, 3.63, 3.82, 4.01$.

different angles of attack with large changes in transition location within a small variation of α .

Pitch oscillations of the airfoil within this α range of sensitive dependence displays a rich variety of unsteady flow phenomena. The flow goes through alternating periods of fully turbulent and laminar flow over the suction side of the airfoil with different governing mechanisms for transition through the oscillating phases. When the flow is mostly laminar over the airfoil surface

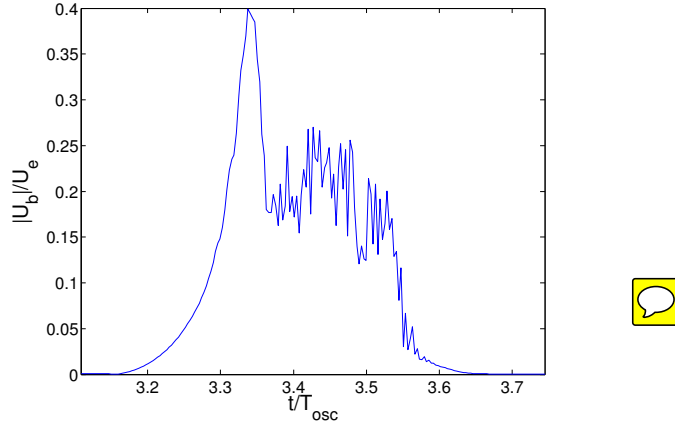


Figure 12: Ratio of maximum reverse flow (U_b) in the leading edge LSB to the boundary layer edge velocity (U_e). 

it separates easily, forming an LSB near the trailing-edge and flow transition occurs over this separated shear layer. As the angle of attack increases, a leading-edge LSB is formed which first excites strongly spatially growing waves causing transition to move upstream. Eventually the LSB reaches a critical size for transition to occur on the separated shear layer, possibly through an absolute/global instability mechanism. In the pitch-down cycle, the reverse phenomenon occurs where the leading-edge LSB shrinks in size and loses its globally unstable character. Such changing dominance of the trailing-edge and leading-edge laminar separation bubbles creates a continuously changing transition point on the suction side. The upstream and downstream velocities of the transition point movement however are vastly different, with an average upstream velocity being around $V_u^{tr} \approx -0.60$ and a much slower downstream velocity of $V_d^{tr} \approx 0.17$. This asymmetry is yet to be investigated, but may be an important parameter in unsteady turbulence modeling, since this point demarcates the regions of turbulent and laminar flow.

5. Acknowledgement

The computations were performed on resources provided by the Swedish National Infrastructure for Computing (SNIC) at the PDC Center for High Performance Computing at the Royal Institute of Technology (KTH). The work was partially funded by European Research Council under grant agreement 694452-TRANSEP-ERC-2015-AdG. The work was also partially funded by Vinnova through the NFFP project UMTAPS, with grant number 2014-00933. We would like to thank Dr. David Eller and Mikaela Lokatt for providing us with the NLF design and the numerous discussions on different aerodynamic aspects of the project.

REFERENCES

- ALAM, M. & SANDHAM, N. D. 2000 Direct numerical simulation of 'short' laminar separation bubbles with turbulent reattachment. *Journal of Fluid Mechanics* **410**, 1–28.
- BRANDT, L., SCHLATTER, P. & HENNINGSON, D. S. 2004 Transition in boundary layers subject to free-stream turbulence. *Journal of Fluid Mechanics* **517**, 1–20.
- CARR, L. W., MCALISTER, K. W. & MCCROSKEY, W. J. 1977 Analysis of the development of dynamic stall based on oscillating airfoil experiments. *Tech. Rep.*
- CHIN, C., NG, H., BLACKBURN, H., MONTY, J. & OOI, A. 2015 Turbulent pipe flow at $Re_\tau = 1000$: A comparison of wall-resolved large-eddy simulation, direct numerical simulation and hot-wire experiment. *Computers and Fluids* **122**, 26 – 33.
- CHOUDHRY, A., LEKNYS, R., ARJOMANDI, M. & KELSO, R. 2014 An insight into the dynamic stall lift characteristics. *Experimental Thermal and Fluid Science* **58**, 188 – 208.
- COORKE, T. C. & THOMAS, F. O. 2015 Dynamic stall in pitching airfoils: Aerodynamic damping and compressibility effects. *Annual Review of Fluid Mechanics* **47** (1), 479–505.
- DONG, S., KARNIADAKIS, G. E. & CHRYSOSTOMIDIS, C. 2014 A robust and accurate outflow boundary condition for incompressible flow simulations on severely-truncated unbounded domains. *Journal of Computational Physics* **261**, 83–105.
- DRELA, M. 1989 *XFOIL: An Analysis and Design System for Low Reynolds Number Airfoils*, pp. 1–12. Berlin, Heidelberg: Springer Berlin Heidelberg.
- DUNNE, R. & McKEON, B. J. 2015 Dynamic stall on a pitching and surging airfoil. *Experiments in Fluids* **56** (8), 157.
- EITEL-AMOR, G., ÖRLÜ R. & SCHLATTER, P. 2014 Simulation and validation of a spatially evolving turbulent boundary layer up to $Re_\theta = 8300$. *International Journal of Heat and Fluid Flow* **47**, 57–69.
- FISCHER, P. F., LOTTES, J. W. & KERKEMEIER, S. G. 2008 nek5000 web page. [Http://nek5000.mcs.anl.gov](http://nek5000.mcs.anl.gov)
- HAMMOND, D. & REDEKOPP, L. 1998 Local and global instability properties of separation bubbles. *European Journal of Mechanics - B/Fluids* **17** (2), 145 – 164.
- HEBLER, A., SCHOJDA, L. & MAI, H. 2013 Experimental investigation of the aeroelastic behavior of a laminar airfoil in transonic flow. In *Proceedings IFASD 2013*.
- HOSSEINI, S. M., VINUESA, R., SCHLATTER, P., HANIFI, A. & HENNINGSON, D. S. 2016 Direct numerical simulation of the flow around a wing section at moderate Reynolds number. *International Journal of Heat and Fluid Flow* **61**, 117 – 128.
- JEONG, J. & HUSSAIN, F. 1995 On the identification of a vortex. *Journal of Fluid Mechanics* **285**.
- LOKATT, M. 2017 On aerodynamic and aeroelastic modeling for aircraft design. PhD thesis, KTH Royal Institute of Technology.
- LOKATT, M. & ELLER, D. 2017 Robust viscous-inviscid interaction scheme for application on unstructured meshes. *Computers & Fluids* **145**, 37 – 51.
- LOMBARD, J.-E. W., MOXEY, D., SHERWIN, S. J., HOESSLER, J. F. A., DHANDAPANI, S. & TAYLOR, M. J. 2016 Implicit Large-Eddy Simulation of a Wingtip Vortex. *AIAA Journal* **54**, 506–518.

- MAI, H. & HEBLER, A. 2011 Aeroelasticity of a laminar wing. In *Proceedings IFASD June 2011*. Paris.
- MCCROSKEY, W. J. 1973 Inviscid flowfield of an unsteady airfoil. *AIAA Journal* **11** (8), 1130 – 1137.
- MCCROSKEY, W. J. 1981 Phenomenon of dynamic stall. *Tech. Rep.*. NASA Ames Research Center; Moffett Field, CA, United States.
- MCCROSKEY, W. J. 1982 Unsteady airfoils. *Annual Review of Fluid Mechanics* **14** (1), 285–311.
- MCCROSKEY, W. J., CARR, L. W. & McALISTER, K. W. 1976 Dynamic stall experiments on oscillating airfoils. *AIAA Journal* **14** (1), 57 – 63.
- MCCROSKEY, W. J., McALISTER, K. W., CARR, L. W. & PUCCI, S. L. 1982 An experimental study of dynamic stall on advanced airfoil sections. volume 1: Summary of the experiment. *Tech. Rep.*.
- MOSER, R. D., KIM, J. & MANSOUR, N. N. 1999 Direct numerical simulation of turbulent channel flow up to $Re_\tau = 590$. *Physics of Fluids* **11** (4), 943–945.
- NATI, A., DE KAT, R., SCARANO, F. & VAN OUDHEUSDEN, B. W. 2015 Dynamic pitching effect on a laminar separation bubble. *Experiments in Fluids* **56** (9), 172.
- PASCAZIO, M., AUTRIC, J., FAVIER, D. & MARESCA, C. 1996 Unsteady boundary-layer measurement on oscillating airfoils-transition and separation phenomena in pitching motion. In *34th Aerospace Sciences Meeting and Exhibit*, p. 35.
- RIVAL, D. & TROPEA, C. 2010 Characteristics of pitching and plunging airfoils under dynamic-stall conditions. *Journal of Aircraft* **47** (1), 80–86.
- SCHLATTER, P., STOLZ, S. & KLEISER, L. 2004 LES of transitional flows using the approximate deconvolution model. *International Journal of Heat and Fluid Flow* **25** (3), 549 – 558, *turbulence and Shear Flow Phenomena (TSFP-3)*.
- SCHLATTER, P., STOLZ, S. & KLEISER, L. 2006 Large-eddy simulation of spatial transition in plane channel flow. *Journal of Turbulence* **7**, N33.
- UZUN, A. & HUSSAINI, M. Y. 2010 Simulations of vortex formation around a blunt wing tip. *AIAA Journal* **48**, 1221–1234.

